# Event-based sub-basalt depth imaging applied to marine seismic data from north of Shetland, UK

Alexander Droujinine, Jan Pajchel & Kenneth Hitchen

Droujinine, A., Pajchel, J. & Hitchen, K. 2008. Event-based sub-basalt imaging applied to marine seismic data from north of Shetland, UK. *Norwegian Journal of Geology* vol 88, pp 167-183. Trondheim 2008. ISSN 029-196X

Seismic wave propagation in media with high-velocity layers (basalts) can be described as an interference of various events commonly referred to as wave types or modes. Proposed here is the event-based processing sequence that enhances and migrates a chosen set of locally coherent arrivals such as PP reflections and mode conversions. While many other events exist, it attenuates most of these other events (e.g. multiples) during pre-processing. The key element is the event separation or mode filtering by means of the Generalized Discrete Radon Transform. This filter is performed by measuring the local Radon-attributes expressed in terms of the wavefront curvature and dip of individual events. Application of these attributes in conjunction with event-based prestack depth imaging methodology onto acquiring conventional 3 km towed streamer data along a 2D profile in the north of Shetland (UK) enables us to accurately delineate volcanic units and imaging beneath high-velocity layers. The main objective is to map the radially-dipping structure of the Erlend pluton and to investigate the potential existence of hydrocarbon bearing Cretaceous layers underneath volcanic units. This case study demonstrates how to produce detailed subsurface images within the region of interest by applying the closely tied processes of prestack event enhancement and separation, well-driven time processing for velocity model building, and final event-based prestack depth imaging. Results show enhanced structural detail and good continuity of principal volcanic units and deeper reflections, suggesting a faulted 0.6-0.9-km-thick succession of Cretaceous rocks in the proximity of well 209/09-1. Our velocity model complements existing low-resolution geophysical models inferred from gravity and wide-angle seismic data.

*Alexander Droujinine, Kenneth Hitchen, British Geological Survey, West Mains Road, Edinburgh EH9 3LA UK. Present address, Alexander Droujinine, Shell International E&P B.V., Kessler Park 1, 2288 GS Rijswijk-ZH, The Netherlands. Jan Pajchel, Norsk Hydro Research Centre, P.O. Box 7190, 5020 Bergen, Norway. (e-mail corresponding author: Alexander.Droujinine@shell.com)*

## Introduction

Volcanic units that cut through the Faeroe-Shetland Escarpment in the North Sea are of interest to the petroleum industry because of their potential for trapping hydrocarbons. A significant number of field and laboratory experiments illustrate the variability in thickness and elastic properties of these units at a variety of scales (Planke et al., 1999; Jolley and Bell, 2002). There are considerable challenges associated with conventional seismic processing in the North Atlantic Margin when the velocity contrast between high-velocity layers (HVLs) and the host medium is large. This is typically the case for layers of the Cretaceous and Tertiary igneous rocks of the British Igneous Province representing igneous centres, extensive sill complexes, and widespread flood basalts (Gatliff et al., 1984; Stoker et al., 1993). In addition to P-wave post-critical phenomena and scattering attenuation typical for realistic basalt structures (Martini and Bean, 2002; Maresh and White, 2005), a great multitude of events (wave types or modes) are generated as seismic waves propagate through HVLs. It appears that the weak sub-basalt PP reflections interfere with strong (water-layer and basalt-related) multiples and converted-wave arrivals caused by dramatic elastic-impedance contrasts between the HVLs and surrounding, relatively soft rocks (Purnell, 1992; Barzaghi et al., 2002; van der Baan et al., 2003). Since the precise mechanism for most of these events varies from case to case, traditional single-event acoustic imaging methodology treats them as undesirable noise to be attenuated in favour of primary PP reflections. On the other hand, a straightforward single-step prestack time migration (PSTM) or prestack depth migration (PSDM) combining all modes (events) is usually not reliable because events migrated with inadequate combinations of velocities produce severe migration artefacts due to frequency-dependent event coupling (Dillon et al., 1988). In practice, interference between various events on prestack gathers always prevents the desired clear separation of events (Martini and Bean, 2002; Spitzer et al., 2003).

To address these problems, one can facilitate event identification before migration via prestack wavefield separation or data pre-conditioning (Dillon et al., 1988) and accomplish event selection during the migration process, as implemented in the event-based processing sequence (Droujinine, 2005). According to the elastic migration principle (Kuo and Dai, 1984), the dataset can be migrated using a combination of velocities and event enhancement amplitude weights restricted to a chosen set of events. This makes it possible to avoid erroneous

processing and misinterpretation of non-PP arrivals as primary PP reflections, without applying labour-intensive pre-processing that involves the use of handpicked mutes (van der Baan et al., 2003) or interactive interpretations based on calculations of the traveltime response (Barzaghi et al., 2002). In event-based migration with accurate velocities, migrated energy from assumed wave-propagation modes coincides with the actual reflector, although different portions of this reflector are imaged with each event (Kuo and Dai, 1984).

In this paper, we apply the above approach to the 2D marine streamer dataset (courtesy of Norsk Hydro) acquired with a standard towed streamer in the basalt-covered area, north of Shetland, UK. The P-velocity model is constrained by good quality sonic logs and check shots. Conventionally, pre-processed data had typical problems for basalt-covered regions like: poor PP signal and strong coherent noise represented by remnants of multiples, refractions and converted waves.

The paper is organized as follows. The Motivation section explains potential benefits of event-based migration exploiting some of the waves that convert upon transmission or reflection in media containing HVLs. The Theoretical Background section and Appendix A briefly outline the key theoretical concepts of event-based Processing Methodology described in the processing methodology section (with the references to Appendix B). In the Geological Setting and Data Analysis sections, we discuss 2D seismic profile, well logs and gravity interpretation from previous studies. In the subsequent section on sub-basalt imaging and results, we present the adopted processing solutions while focusing on each step of the workflow. A chief consideration when processing seismic data in the area of interest is to derive an accurate, anisotropic velocity model using measured local wavefront attributes (Appendix A) and calibrated well data.

## Motivation

Previous modelling studies (Purnell, 1992) suggest that the large velocity contrast at the top basalt should be an efficient generator of converted waves that follow either symmetric or asymmetric paths. If recorded, this data might be suitable for successful delineation of individual basalt lava flows and improved overall sub-basalt illumination. To illustrate the concept, we consider an idealized two-layered model of HVL. In Figure 1a, absolute values of plane-wave reflection and transmission coefficients for PP and PS waves are compared at the top of the basalt interface. Because of the similarity of S-wave velocity of HVL and the P-wave velocity of the overlying structure, PS conversion is quite efficient at incidence angles beyond the critical angle of 30° or offset of 1.35 km (cf. Figures 1a and 1b). For typical PS-wave stacking angles of 30-40° (Figure 1a) or offsets of 1.35-1.96 km (Figure 1b) the converted-wave reflectivity is expected to produce a reflection coefficient of about 0.8. At pre-critical angles of incidence, P-wave transmission is the most energetic process. However, beyond the critical angle up to the maximum recorded incidence angle of 52° or offset of 3 km (cf. Figures 1a and 1b), almost no P-wave energy is transmitted, while PS-wave transmission energy becomes nearly equal to the PP-wave transmission energy at near offsets. Thus, this simple example explains why converted mode energy could be an increasingly strong component of the wave field reflected from within and below basalt at all offsets greater than the critical distance at the top basalt.

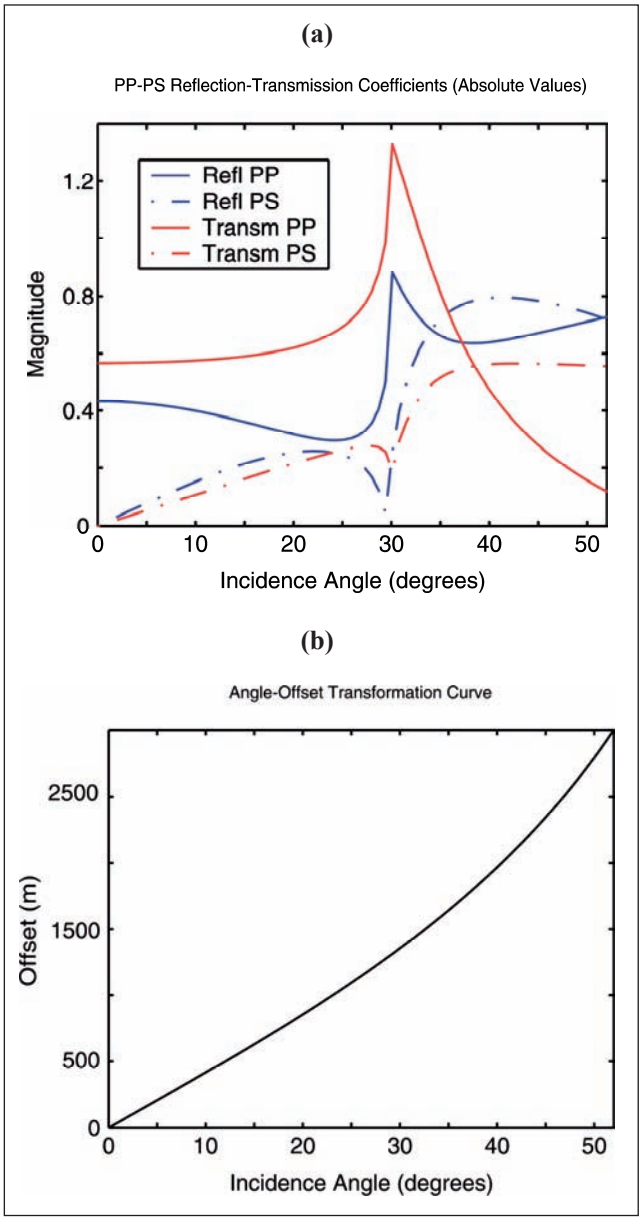


*Figure 1: (a) Plane-wave PP and PS reflection and transmission coefficients as functions of the incidence angle and (b) relationship between the incidence angle and offset given by the angle-offset transformation curve for the top of basalt (layer 2). The effective elastic parameters are as follows: $V_{p1}$ = 2.134 km/s, $\rho_1$ = 1.9 g/cm$^3$, $V_{p2}$ = 4.268 km/s, $\rho_2$ = 2.4 g/cm$^3$, and $V_p/V_s$ =1.85. The reflector depth of 1.172 km (top of basalt) is taken from the sonic log data in Figure 6a.*

## Theoretical background

One of the key issues of event-based (e.g. converted-wave) processing is identifying the correct events and carrying out velocity analysis. In practice, strong multiple reflections and post-critical refractions with complex ray paths render prestack identification of individual events complicated. Since the converted-wave effective velocity is close to that of multiples, it is difficult to attenuate multiples while retaining the mode conversions.

In this paper, we address the above problems by applying the event-oriented approach that relies on signal enhancement and wavefield separation in prestack domains. Much of the methodology that follows was motivated by earlier work of one of the authors of this paper (Droujinine, 2005). He derived and tested numerically the Generalized Discrete Radon Transform (GDRT) suitable for imaging beneath HVLs. This is essentially a beam-forming method that employs a procedure of delay-and-sum local slant stack processing to steer a local parabolic beam

$$t(x_0, X) \approx \tau + P(X_0)(X - X_0) + Q(X_0)(X - X_0)^2 \quad (1)$$

with the coefficients

$$P(X) = \frac{\partial t(X)}{\partial X} \text{ and } Q(X) = \frac{1}{2}\frac{\partial^2 t(X)}{\partial X^2} \quad (2)$$

in a particular direction over a range of offsets $X$ in the vicinity of $\tau = t\ (x_0, X_0)$ and $X = X_0$. In this case, $x_0$ is the $x$-coordinate of a reference point in the proximity of the observation (CMP, source or receiver) point. Firstly, we estimate the local linear moveout

$$t(x_0, X) - \tau = P(X_0)(X - X_0) \quad (3)$$

wherever the steering beam half-width aperture is sufficiently small as $X - X_0$ (typically, a five-to-ten-trace beam aperture is sufficient). Secondly, the local linear moveout

$$\Delta t(x_0, X) = t(x_0, X) - \tau - P(X_0)(X - X_0) = Q(X_0)\tilde{X} \quad (4)$$

in the domain $\{\tau, \tilde{X} = (X - X_0)^2\}$ enables us to estimate the wavefront curvature attribute $Q(X_0)$ if the beam aperture is not small (e.g. a twenty-trace bin size can be used). Thus, we transform original traces $\{t, x, X\}$ into a set of beam-stacked traces $\{\tau, x_0, P(x_0), Q(x_0)\}$. This transformation needs to be computed for each sample in an input trace.

The $P$-$Q$ attribute analysis based on eqs. (1)-(4) produces local slant stacks by summing traces over a certain range of spatial variables such as $x$ (location) or $X$ (offset). Specifically, we cross-correlate the input traces and translate the cross-correlation lag into the local Radon-attributes given by eq. (2) that can be used to compute velocity and reflection time updates. A good demonstration of GDRT is to examine a simple 1D case of constant vertical velocity gradient when most seismic reflection traveltimes with symmetric paths can be approximated by hyperbolas (see Figure 2). As depicted in Figure 2a, the hyperbolic moveout equation describes the reflection traveltime as a surface in the $\{\tau_0, X\}$ domain, where $\tau_0$ is the intercept (zero-offset) two-way time. Figures 2a and 2b show the estimated local event slope and curvature attributes representing the $P$-$Q$ attribute surfaces in the offset-time domain. In practice, the $P$-$Q$ attributes are mapped directly from the data using eq. (1), as discussed in Appendix A.

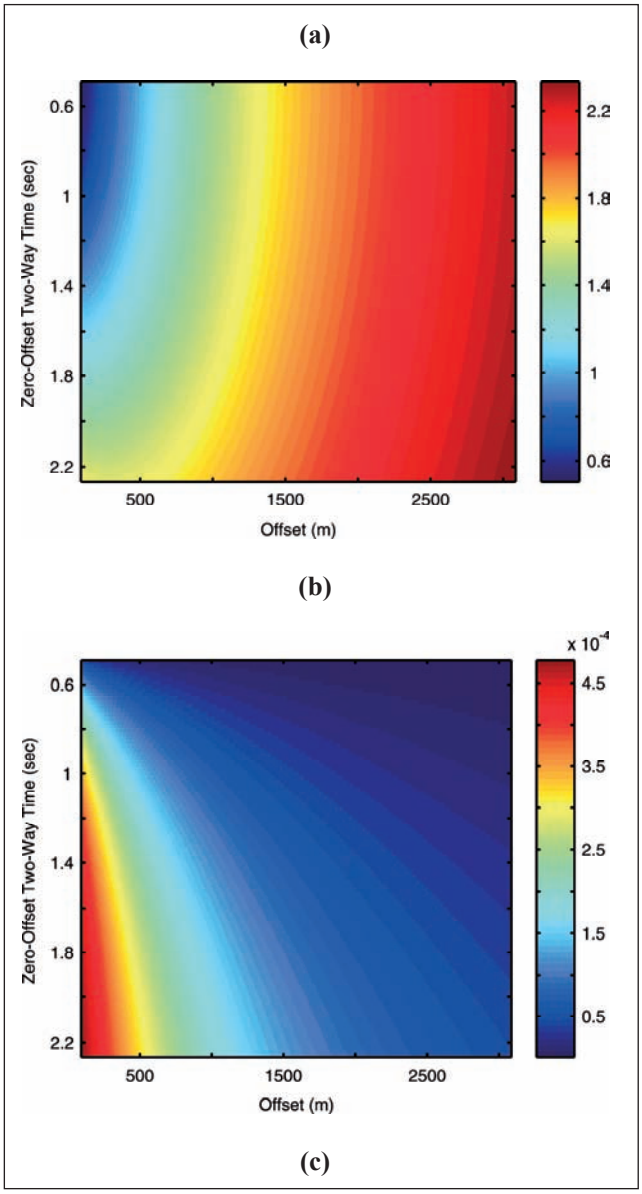


*Figure 2: The expected 1D linear velocity profile for clastic sediments (Ogilvie et al., 2001): (a) traveltime surface (hyperbolic moveout in sec), (b) P-attribute (in s/m) and (c) Q-attribute (in s/m²). The RMS velocity function is $V_{RMS}$=1693 - 0.6033$z$ (in m/s), where $z$ is the depth below sea floor in meters.*

## Processing methodology

Figure 3 summarizes the following essential steps of our wave mode dependent processing sequence: (1) prestack data enhancement (phase deconvolution, surface-related multiple attenuation, etc.) and GDRT wavefield separation (see section on theoretical background and Appendix A); (2) iterative 2D PSTM as a part of time-domain

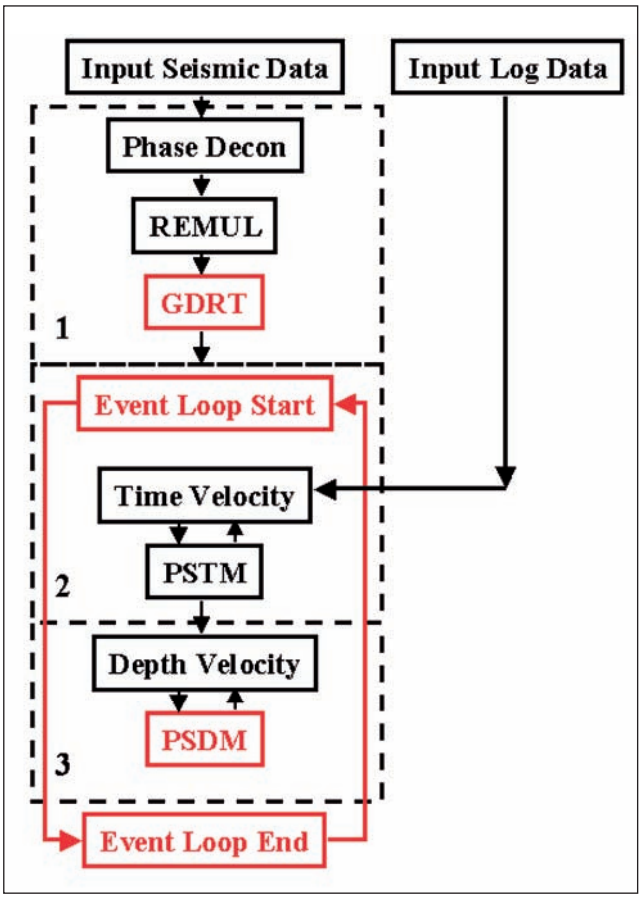


*Figure 3: Flow chart of event-based processing workflow: (1) data pre-processing (prestack signal enhancement and wavefield separation); (2) velocity analysis and velocity model building; (3) PSTM and subsequent PSDM runs. Standard processing steps are phase deconvolution, multiple attenuation using the "REMUL" program created within Norsk Hydro (Lokshtanov, 1999), seismic-well tie, time-domain velocity model building, zero-offset time-to-depth mapping, and depth-domain migration velocity analysis.*

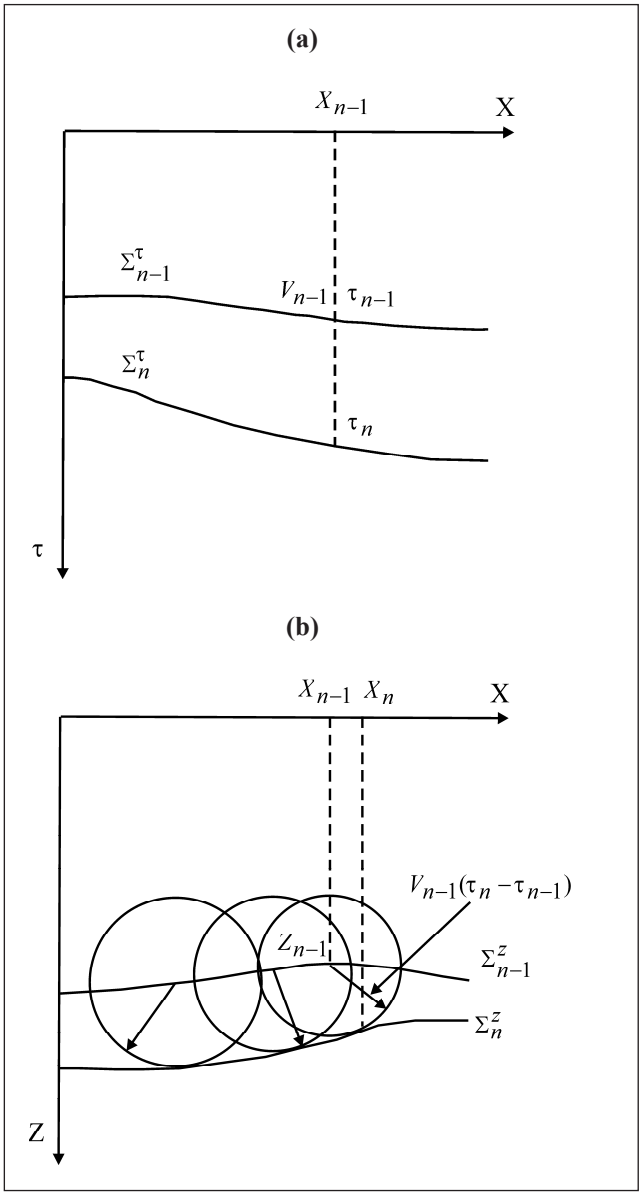


*Figure 4: Sketch of zero-offset time-to-depth mapping based on the kinematic Huygens' principle: (a) time-domain stacked or migrated section with picked horizons $\Sigma^{\tau}_{n} : \tau_n(X)$ $(X = X_n)$ and (b) depth-domain stacked or migrated section with picked horizons $\Sigma^{z}_{n} : Z_n(X_n)$.*

model building calibrated by well logs and regional velocity trends; (3) accurate time-to-depth mapping (see Figure 4 and Appendix B) and subsequent PSDM model updates based on the output of phase 2.

*Data Pre-Processing*

The objective of prestack signal enhancement and wavefield separation is twofold: (1) signal enhancement (noise suppression and increasing the overall signal-to-noise ratio) and (2) GDRT separation of the key events listed in Table 2. First of all, the recorded traces are converted to a zero phase band-limited signal applying a deterministic zero phasing. Zero phase signature processing is then carried out in order to remove the reverberation effects due to ghosts. Calculation of both filters is based on the post-stack autocorrelation wavelet. Initial multiple attenuation tests involve linear Radon and $\tau$- $p$ deconvolution (Spitzer et al., 2003). The aim of subsequent GDRT filtering is to filter out the unwanted waveforms and to recover the desired signal. The single pass of GDRT is implemented as follows:

(1) Divide the input gather into small ($\tau$- $X$) segments and apply the forward GDRT for every segment.

(2) In the local ($\tau$- $P$ - $Q$) domain, we pick the most dominant $P$ and $Q$ values corresponding to strong unwanted events, and inverse transform these values into the ($\tau$- $X$) domain. This yields the noise model segment containing refractions (events H1 and H2) as well as global (asymmetric) mode conversions C1 (see Table 2).

(3) Subtract the noise model from the input segment in the least-squares sense after trace matching (White, 1980).

The output gather is obtained by repeating steps 1-3 for all the segments. Note that the GDRT preserves amplitudes and waveforms but can be severely aliased if the Nyquist condition of optimal spatial sampling is violated.

Table 1 Acquisition parameters of the seismic survey.

| | |
|---|---|
| Acquisition | Towed streamer |
| Area | North of Shetland |
| Company | Norsk Hydro |
| Year | 1994 |
| Number of shots | 2155 |
| Number of receivers | 240 |
| Number of traces | 517200 |
| Min offset (m) | 95 |
| Max offset (m) | 3083 |
| Shot spacing (m) | 25 |
| Receiver spacing (m) | 12.5 |
| Record length (sec) | 3.5 |

Therefore, windows derived from semblance data limited certain pass band (typically, 15-50 Hz) should be multiplied with the original GDRT to eliminate alias contributions while still including undistorted GDRT waveforms.

*Reference Velocity Model*

The velocity model building for prestack migration in the area has two equally important tasks – the preliminary interpretation of the complicated HVLs and the sediment velocity changes around and beneath these units. Following Robein and Hanitzsch (2001), RMS velocity analysis is initially applied to the CMP data based on the velocity approximation $V(x,\xi) = V_0(\xi) + \Delta V(x,\xi)$. Here, $V_0(\xi)$ is the one-dimensional guide function derived from the sonic logs and constrained by the regional regression formula (Ogilvie et al., 2001); the velocity perturbation $\Delta V(x,\xi)$ is a given function of lateral and vertical coordinates $x$ and $\xi = t$ (time) or $\xi = z$ (depth).

In order to estimate this velocity perturbation, two locked window displays are used. The first window shows the moveout-corrected CMP gather on the vertical time axis (T0 in ms) and the second one shows the semblance RMS velocity panel. Semblance velocity scans are generated at given CMP locations (e.g. every 500 m), with the central velocity function corresponding to the velocity $V_0$. At locations where the moveout-corrected CMP gathers do not demonstrate optimal flattening, a residual moveout correction can be picked and applied. These changes are shown on the semblance display. The gathers and semblance displays can also be used to check that the model contains a sufficient number of surfaces to define the velocity variation of the data properly. If the gathers show good flattening at the top and base of a layer but not at intermediate points, this indicates that the layer should be sub-divided so that different velocities can be applied.

If the model contains steep dips and/or strong lateral velocity contrasts, then the velocity V(x, ξ) may no longer be estimated correctly. In these cases, structural updating is necessary. In most cases, this can be achieved adequately by using the latest model for migration of an unmigrated time stack volume, upon which a structural re-interpretation can be performed. In cases of extreme complexity, as for example in this study, imaging below HVLs, the RMS velocity analysis may not give sufficient confidence of the optimal focusing and correct structural positioning. It is then necessary to use prestack time and depth migration runs for a series of shot or CMP gathers,

Table 2 Key to the notation used in many of the figures.

| Symbol | Definition |
|---|---|
| PP | Primary PP reflection. |
| WB | Water-bottom reflection. |
| P | PP reflection from the base of Pliocene. |
| O | PP reflection from the base of Oligocene. |
| EO | PP reflection from the top of Middle Eocene. |
| TB | PP reflection from the top of basalt (Top of Basic Volcanics). |
| BB | PP reflection from the base of basalt (Base Tertiary Unconformity) that can interfere with the asymmetric P-to-S mode conversion PPSP at the TB interface. |
| C1 | Group of events containing PPSP (downgoing P wave and upgoing S wave with conversion to P wave at the sea floor) arrivals associated with high-contrast interfaces and overprinted by surface-related or water-layer peg-leg multiples. PPSP events and multiples are separated during event-based PSDM. |
| C2 | Group of events containing PSPPSP (symmetric local mode conversion at the TB and BB interfaces during transmission, S travelling inside basalts) arrivals overprinted by inter-basalt and peg-leg multiples. Along the PSPPSP path, a wave converts from S to P upon exiting the basalt and from P to S upon re-entering the basalt (Purnell, 1992). PSPPSP events and multiples are separated during event-based PSDM. |
| M | First-order water-bottom (PPPP) multiple suppressed during event-based PSDM. |
| H, H1, H2 | Refracted arrivals (head waves and corresponding peg-leg multiples, diving waves, etc.) that arrive ahead of PP reflections (including the water-wave cone) at larger offsets. These events represent noise. |

which can then be structurally re-interpreted and interpolated to update the reference model.

The key step of the time-domain reference velocity model building is to apply the conventional Dix inversion to the stacking velocity field. Due to well-known uncertainties of Dix inversion (Lambaré et al., 2007), we focus our attention on calibration between wells and seismic sections. Firstly, we build an initial isotropic velocity model, using existing well control and time horizon maps consistent with the available lithology columns. Secondly, we estimate the effective Thomsen's (1986) parameter δ from the mismatches between effective P-wave velocities derived from surface seismic data after signal enhancement and compressional sonic logs after upscaling. Since the lack of structure permitted the assumption of a vertical axis of symmetry (VTI), we incorporate the following velocity matching formula (Hawkins et al., 2001)

$$V(\text{flat dip}) = V_0\sqrt{1+2\delta}\,, \qquad (5)$$

where $V$ is the effective, normal moveout (NMO) or image-ray velocity and $V_0$ is the vertical velocity predicted by calibrated sonic logs and check shots. Although the meaning of δ is less obvious than that of other anisotropy parameters, it has a clear formal definition, relating to the second derivative of the phase velocity function at normal incidence to the vertical P-wave velocity (Thomsen, 1986, 1999). Since the first derivative of phase velocity at normal incidence is zero, δ is responsible for the angular dependence of phase velocity in the vicinity of vertical axis.

Evidently, confidence limits $\pm\Delta\delta$ of the parameter δ depend on the quality of the seismic-well tie and have nothing to do with the horizontal velocity. Under the short spread assumption ($X/z<1$) and weak lateral velocity variations ($|\Delta V(x,\xi)|/V_0(\xi) << 1$), the VTI moveout is still hyperbolic and is controlled by only the parameter δ (Thomsen, 1986). Hence, the initial values of δ can be checked by running "sensitivity tests" with moveout-corrected CMP gathers for inspection of their flatness. All these tests are evaluated for the given subset of CMP gathers and a revised anisotropy parameter grid is calculated over the target region. This grid can then be subjected to edits and smoothed as for the initial model loading.

### *Prestack Time Migration*

The time processing procedure remains the important step in our sequence because the quality of the final depth image is strongly related to the quality of stacks or time migrated sections (Yilmaz, 2001; Robein and Hanitzsch, 2001). In the present study, this process is tailored to build a reference model beyond the layered Earth assumption and to carry out prestack migration velocity analysis in the time domain. Specifically, we start from picking the key horizons on a time migrated section obtained with a migration velocity $V_{mig}$. The better the image of the time migrated section, the better the depth-domain velocity model. When there is no strong heterogeneity and high dips, reflectors are imaged at the zero-offset time $\tau_0$ (Figure 4a) and $V_{mig}$ is close to the stacking velocity $V_{stack}(t=\tau_0)$. Once $V_{stack}$ has been determined during pre-processing, the pre-processed subsets are migrated several times, using conventional Kirchhoff PSTM (e.g. Robein and Hanitzsch, 2001) for major wave types identified during pre-processing (see above section on data pre-processing), as outlined by Barzaghi et al. (2002). We consider a smooth 2D model for which we search for the principal reflectors after PSTM has been applied with the velocity $V_{mig}=V_{stack}$. This leads in general to non-flat image gathers and requires additional (e.g. one or two) passes of PSTM with updated $V_{mig}$ until we reach the optimum flatness. Since the imaging is kept in the time domain, relative insensitivity to errors in $V_{mig}$ results in a moderate loss of focusing.

### *Prestack Depth Migration*

In contrast to PSTM, PSDM is a more accurate migration that is much more sensitive to the choice of migration velocity. Therefore, it needs many stages of migration velocity updating and migration before proceeding through final interpretations (Jones, 2003). At least three iterations are necessary to obtain a reliable PSDM velocity model:

1. Of particular importance is the need to incorporate the key time horizons (output of PSTM) into the reference interval velocity model that accounts for all available sources of velocity and geological information. At this stage, time stacking velocities are converted to interval velocities and then to depth interval velocity via zero-offset time-to-depth mapping described in Appendix B. With horizon intervals and depth interval velocities a velocity grid $V^{(0)}$ is constructed and used for the initial PSDM (step 1).

2. The output of step 1 helps interpreters to identify the HVLs in the depth domain in order to reduce uncertainties of the time-domain interpretation (Lambaré et al., 2007). It is then possible to generate the final depth-domain top basalt and base basalt interfaces (Figure 4b) and to create the modified velocity field $V^{(1)}$. Here, we make use of the velocity $V^{(1)}$ to compute depth migrated post-stack volume and depth migrated prestack volume (step 2) to facilitate velocity updating beneath base basalt. Note that although detailed interpretation of volcanic units is essential to capture the rugosity of basalts in the region (Planke et al., 1999; Ogilvie et al., 2001), the depth-converted horizons (Figure 4b) should be cleaned by filtering out cycle skips and filling the gaps by extrapolating from well-conformed portions of each horizon.

3. A short-wavelength refinement of the velocity field $V^{(1)}$ is then carried out in the post-migrated domain

through the Residual Moveout (RMO) analysis of common image gathers by performing velocity scans in the areas of low signal-to-noise ratio, especially beneath the base basalt horizon. As part of the updating process, bending ray tracing occurs for the subsurface locations where the RMO corrections were picked (Jones, 2003).

The iterative method of migration and velocity updating is repeated until the following three conditions are met: an acceptable depth image is observed consistent with available *a priori* information; focusing energy and overall signal-to-noise ratio are optimised; and primary reflections are flattened on associated image gathers.

As far as the implementation of PSDM is concerned, the beam-type GDRT depth migration procedure (Droujinine, 2005) related to the fast wavepath or Fresnel-aperture PSDM (Tabti et al., 2004) is utilized to provide depth images for model building as well as for the final output over the region of interest. This procedure is applied to map the reflections to their true vertical depth locations ($z$, $\xi$) for both PP and converted P-to-S-to-P waves (see Table 2). As with conventional elastic Kirchhoff PSDM (Kuo and Dai, 1984), the two key migration steps are as follows: (1) calculation of multi-wave-type traveltimes between the image points ($z$, $\xi$) and observation points; (2) using these traveltimes to map the reflections to the image points. Input data are pre-processed shot gathers after GDRT wavefield separation, followed by traveltime computations in terms of local wavefront attributes (2).

## Geological setting

The overall objective of our study is to consider evidence for the depositional environment of the strata of the Erlend Volcano (Figure 5) revealed by seismic reflections. The Erlend Tertiary plutonic centre to the north of Shetland consists of a buried, partially-eroded shield volcano underlain by a basic pluton. Unlike the related UK onshore central volcanic complexes, it retains a reasonably complete succession of volcanic lithologies (Stoker et al., 1993). Analysis of geophysical data (Gatliff et al., 1984) has shown that there is a lava escarpment that is interpreted as a hyaloclastite deltaic sequence which formed as lavas entered the basin, chilled out and fragmented, producing a prograding sequence of bedding volcanic breccias. The basalts of late Palaeocene age (Stoker et al., 1993) provide strong reflections that can be traced across the Faeroe-Shetland Trough into the

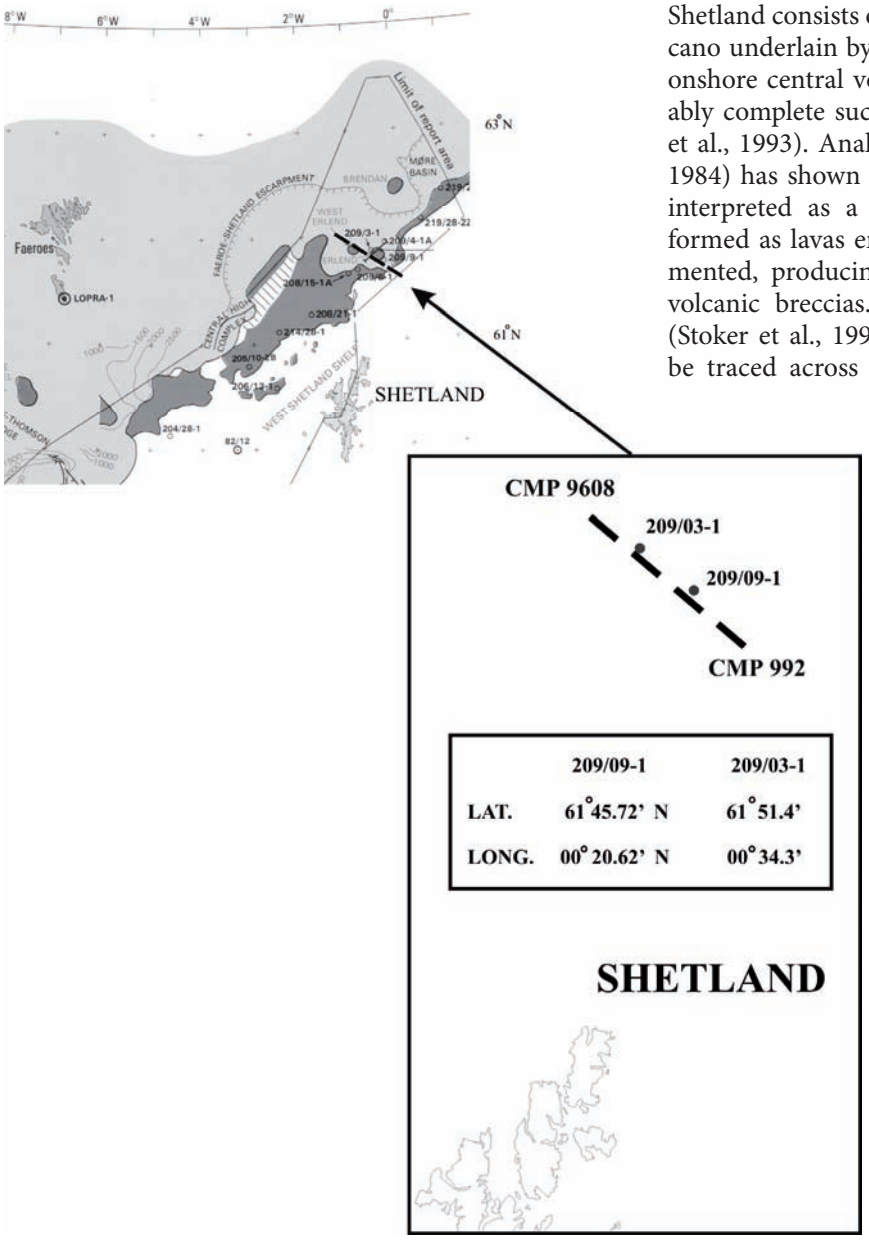


*Figure 5: Study area (UK sector of the North Sea, quadrants 208 and 209): geological map of the Faeroe-Shetland Escarpment (FSE) (courtesy of BGS, see also Gatliff et al., 1984), well locations (the deep borehole on land LOPRA-1, the BGS borehole 82/12, and commercial wells) and schematic CDP locations for the GWS94 profile (CDP 992-9608), and (d) enlarged schematic illustration of the GWS94 survey geometry (well locations along the line are depicted). Grey light-coloured region indicates Tertiary igneous rocks at subcrop. Grey dark-coloured areas designate the Møre Basin / Faeroe-Shetland Basin sill complex and igneous centres including the Erlend Volcano. Oblique solid straight lines denote the axial opaque zone. Depth contours (in metres) of the top-basalt boundary are shown.*

northern parts of quadrants 208 and 209 (Figure 5). Several hydrocarbon exploration wells (Figure 5) have penetrated thick sequences of subaerial facies basaltic lavas and subaqueous volcanic breccias, overlying Palaeogene and Cretaceous sedimentary rocks interbedded with medium to fine-grained silicic igneous rocks (Stoker et al., 1993; Jolley and Bell, 2002).

## Data analysis

We begin with the analysis of available input seismic, gravity and well data. A logical sequence consists of a systematic progression from well log conditioning to seismic QC (including spectral analysis) and finally preliminary identification of some events listed in Table 2. This includes initial model building with particular attention paid to gravity interpretation (Gatliff et al., 1984) and the recent regional studies (Planke et al., 1999; Ogilvie et al., 2001).

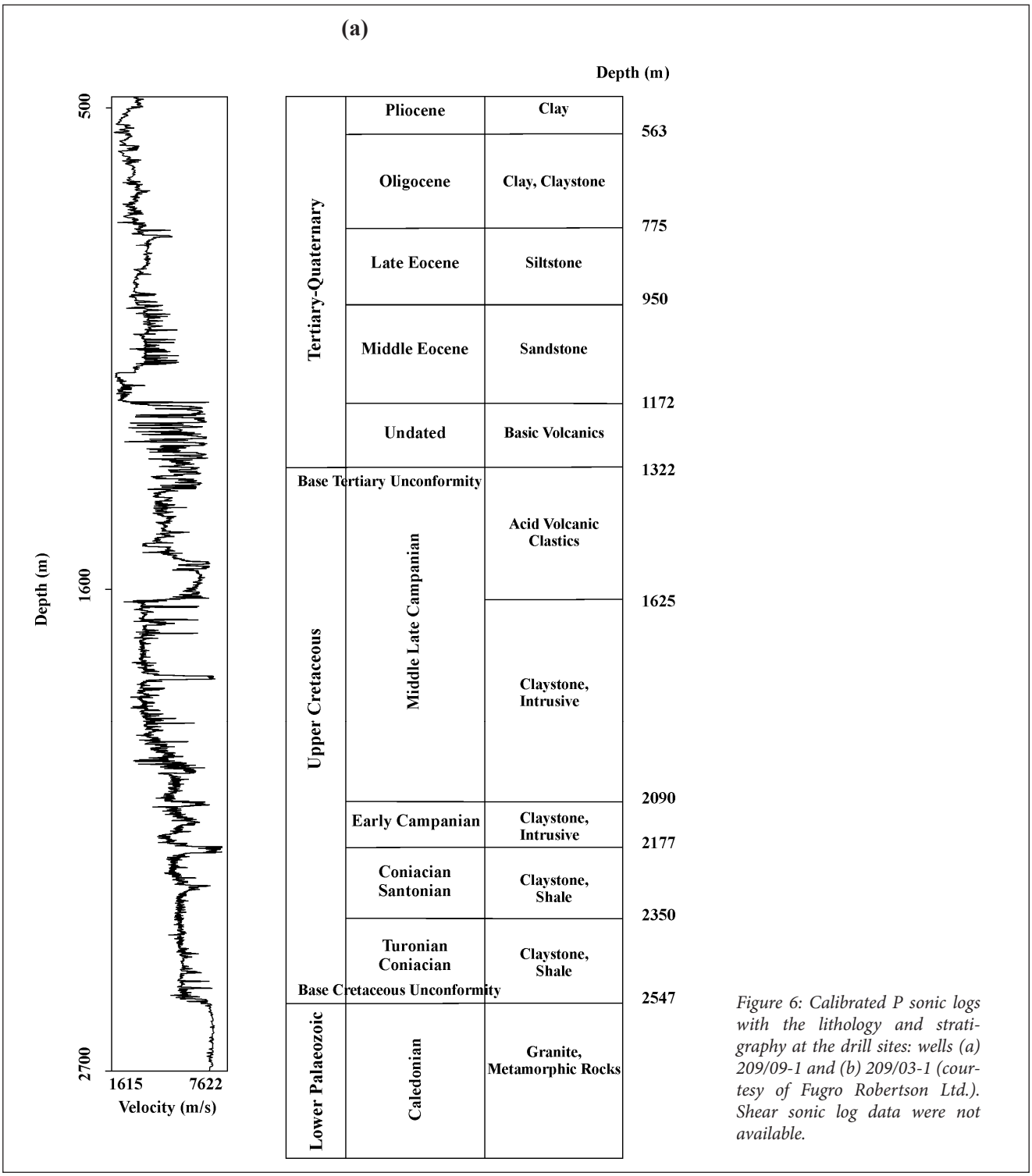


*Figure 6: Calibrated P sonic logs with the lithology and stratigraphy at the drill sites: wells (a) 209/09-1 and (b) 209/03-1 (courtesy of Fugro Robertson Ltd.). Shear sonic log data were not available.*

*Well Data*

Interpreted wireline logs from wells 209/09-1 and 209/03-1, on the SE and NW flanks of the former volcano, showed the presence of total volcanic successions over 453 m of basic and acid volcanic rocks and 836 m of pyroclastic extrusive rocks, respectively (compare Figures 6a and 6b). Jolley and Bell (2002) provided a detailed analysis of the igneous lithologies encountered in these wells. Figure 6a confirms 150 m, from 1172 m to 1322 m below rotary table (RT), of basic volcanic rocks as well as 303 m, from 1322 m to 1625 m below RT, of acid volcanic clastic rocks, together with siltstones and sandstones. The check-shot time-depth pairs were used to "tie" sonic logs to the seismic data (Figure 7). Figure 8 shows that the clastic velocity-depth curve
$V_0 = 1700(\pm 10) + 0.511(\pm 0.09)z$ (linear regression fit)
derived from sonic logs and check-shots (Figures 6a and 7). It is seen that this curve is nearly identical to that of Ogilvie et al. (2001).

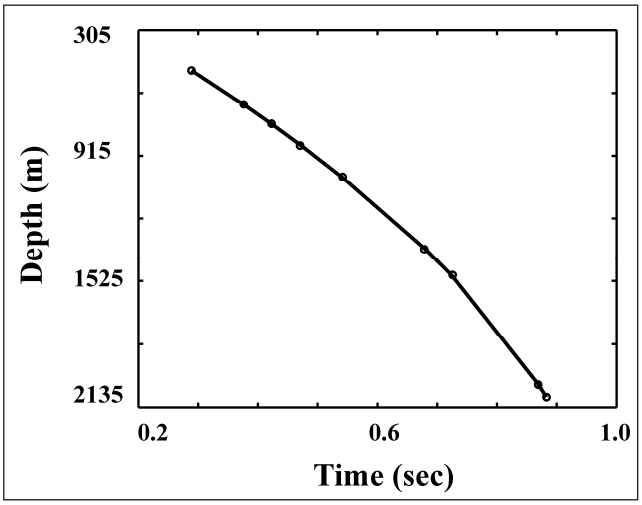


*Figure 7: Vertical-incidence time-to-depth relationship very near well 209/09-1: (a) check-shot (one-way) time-depth pairs (circles) and their polynomial fit (solid line) with the error range 0.02-2.25 ms.*

*Seismic Data*

The marine streamer dataset was acquired with standard towed streamer over offsets of traditional length. Details of 2D acquisition can be found in Table 1. The dataset was provided by Norsk Hydro after standard signal enhancement including source deconvolution and free-surface multiple attenuation. This is prior to our data pre-processing procedure. The data (multi-offset traces) acquired for a single shot is initially arranged in a common-shot gather (Figure 9). In Figure 9a (T-X display), one can identify and correlate the prominent reflections (events WB, P, O, TB, and BB in Table 2) as well as high-amplitude coherent noise (refractions H and multiples M). The spectral characteristics of recorded common-shot data were examined through F-X power spectra (Figure 9b) and average power spectra (Figure 9c) for selected subsets of traces. The F-X spectrum in Figure 9b shows the frequency-dependent amplitude dimming at near and mid-range offsets. This is possibly due to some roughness of HVL boundaries at a scale similar to the seismic wavelength (Martini and Bean, 2002; Maresh and White, 2005). Attenuation of seismic energy within the HVLs caused by internal multiple scattering (Spitzer et al., 2003) is another mechanism that may explain the above amplitude dimming effect. The F-X spectrum in Figure 9b also shows the increase of amplitudes at large offsets. According to modeling examples of Spitzer et al. (2003), this is likely to be the contribution of converted-wave energy (P-to-S conversion at the TB boundary). In Figure 9c, the spectrum contains little energy above 70 Hz and below 10 Hz. The spectrum is flattened to within 5 dB from 15-50 Hz. To account for poor data quality and acquisition limitations we apply a processing sequence that attenuates both coherent and random noise by preserving the frequency content illustrated in Figures 9b and 9c.

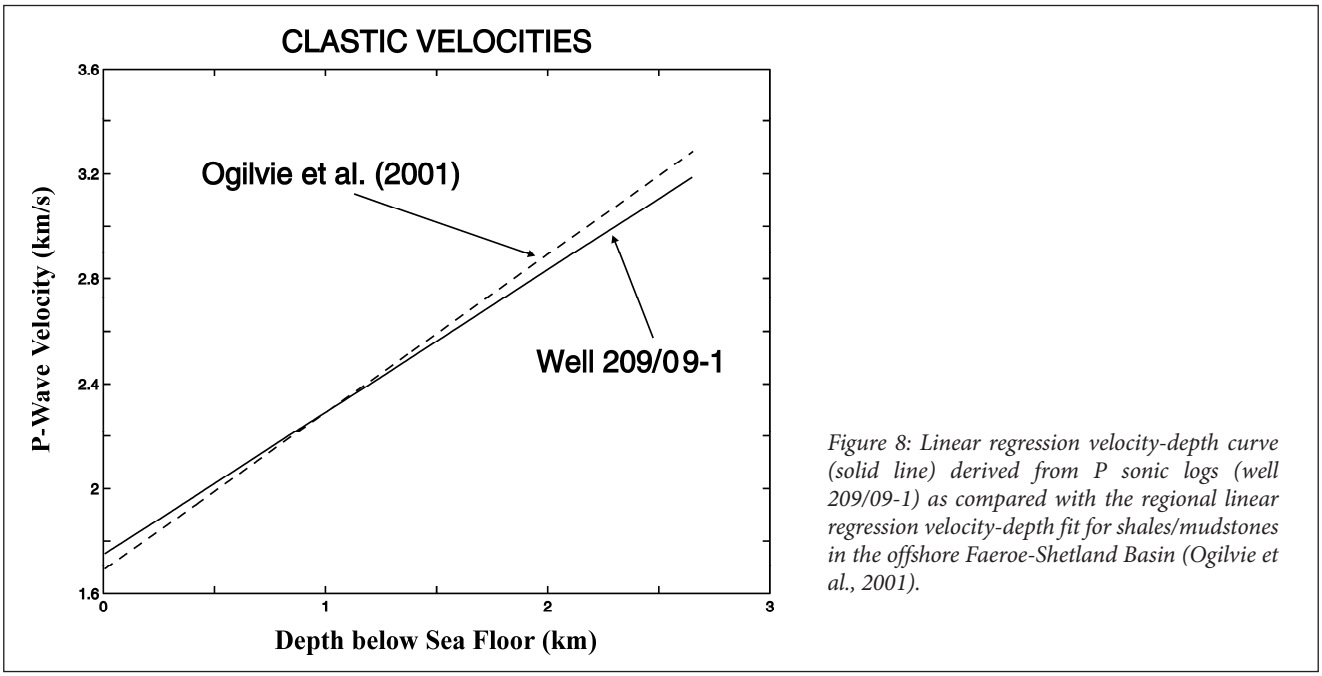


*Figure 8: Linear regression velocity-depth curve (solid line) derived from P sonic logs (well 209/09-1) as compared with the regional linear regression velocity-depth fit for shales/mudstones in the offshore Faeroe-Shetland Basin (Ogilvie et al., 2001).*

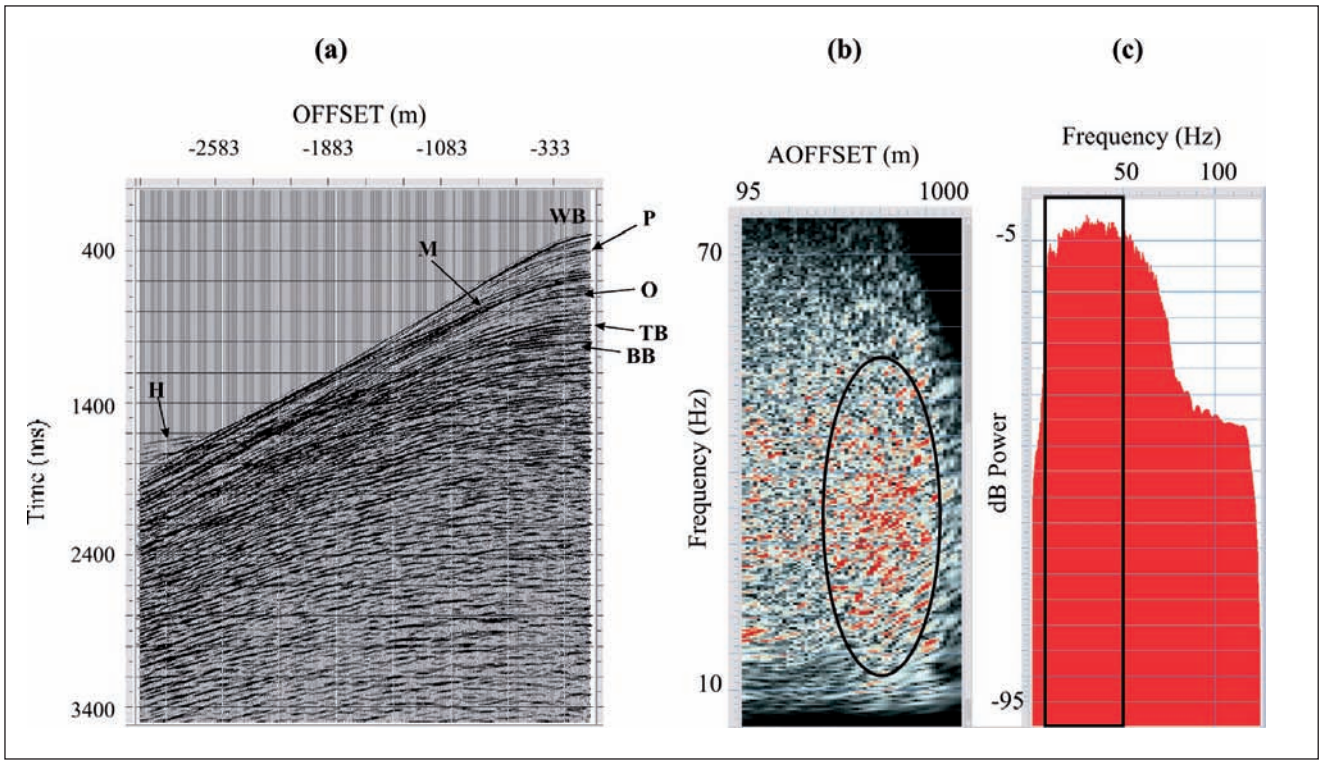


*Figure 9: Example single shot gather (CMP=992) before our data processing: (a) T-X display (coordinate axes are two-way time and negative offset), (b) F-X spectrum as a function of frequency and absolute offset (colour means energy power in dB: black colour corresponds to the minimum energy and red colour corresponds to the maximum energy), and (c) average power spectrum (in dB) computed directly from the autocorrelation of common-shot traces. The high-amplitude area is enclosed by the ellipse (middle panel). The rectangle indicated by solid lines fits the useful frequency bandwidth (right panel). The total signal bandwidth equals, or slightly exceeds, 100 Hz. Event notations are described in Table 2.*

*Non-Seismic Data*

The regional distribution of the Tertiary basalts in the study area was postulated by interpretation of Western Geophysical and BGS marine gravity data as a provisional free air gravity anomaly mapped at a scale of 1:50000. Results of the 2D gravity modelling with the RMS error of less than 1 % have also allowed us to elucidate the structure of the Erlend complex. From the observed and calculated gravity profiles, a stripped-free air gravity anomaly map was produced representing the observed gravity, corrected for the effect of the seawater and the basalts. Seismic-gravity interpretation confirmed that depositional dips within the basalts could approach 45°. See Gatliff et al. (1984) for details.

## Sub-basalt imaging results

Referring to the flowchart in Figure 3 and the above processing methodology section, we apply our methodology to the 2D field dataset acquired in the north of Shetland (see Figure 5 and our subsection on seismic data).

*Data Enhancement and Wavefield Separation*

Figure 10a shows an example of prestack T-X domain shot gather prior to GDRT wavefield separation. It contains the source signals (waveforms), some of which we would like to retrieve (e.g. primary PP reflections in near-offset range and some non-PP arrivals in mid-offset range). Following the steps outlined in our pre-processing subsection, we apply the forward GDRT to the input gather in Figure 10a (step 1) and pick the dominant events representing coherent noise in the ($\tau$ - $P$ - $Q$) domain (step 2). This yields the noise model segment containing refractions (events H1 and H2) as well as global (asymmetric) mode conversions C1, as indicated in Figure 10b. The output gather in Figure 10c is obtained by repeating steps 1-3 outlined in the `data pre-processing´ subsection for all local ($\tau$ - $X$) segments whose superposition yields the input traces in Figure 10a. A comparison of Figures 10a and 10c shows that the process of GDRT filtering enhances spatial continuity of either PP or non-PP (C2) reflection energy while suppressing undesired events at near- or mid-offsets. Although cross-talk artefacts and remnants of more complicated paths are still observed in Figure 10c, it is reasonable to assume that they will be negligible in the depth migrated domain. For the sake of comparison, Figure 10d portrays the result of applying the Parabolic Radon Transform (PRT) algorithm to the same data traces (after Spitzer et al., 2003). As can be seen by comparing Figures 10c and 10d, while both GDRT and PRT procedures have been effective in suppressing the strong refraction H1, it appears that PRT filtering enhances also arrivals C2 and refractions H2.

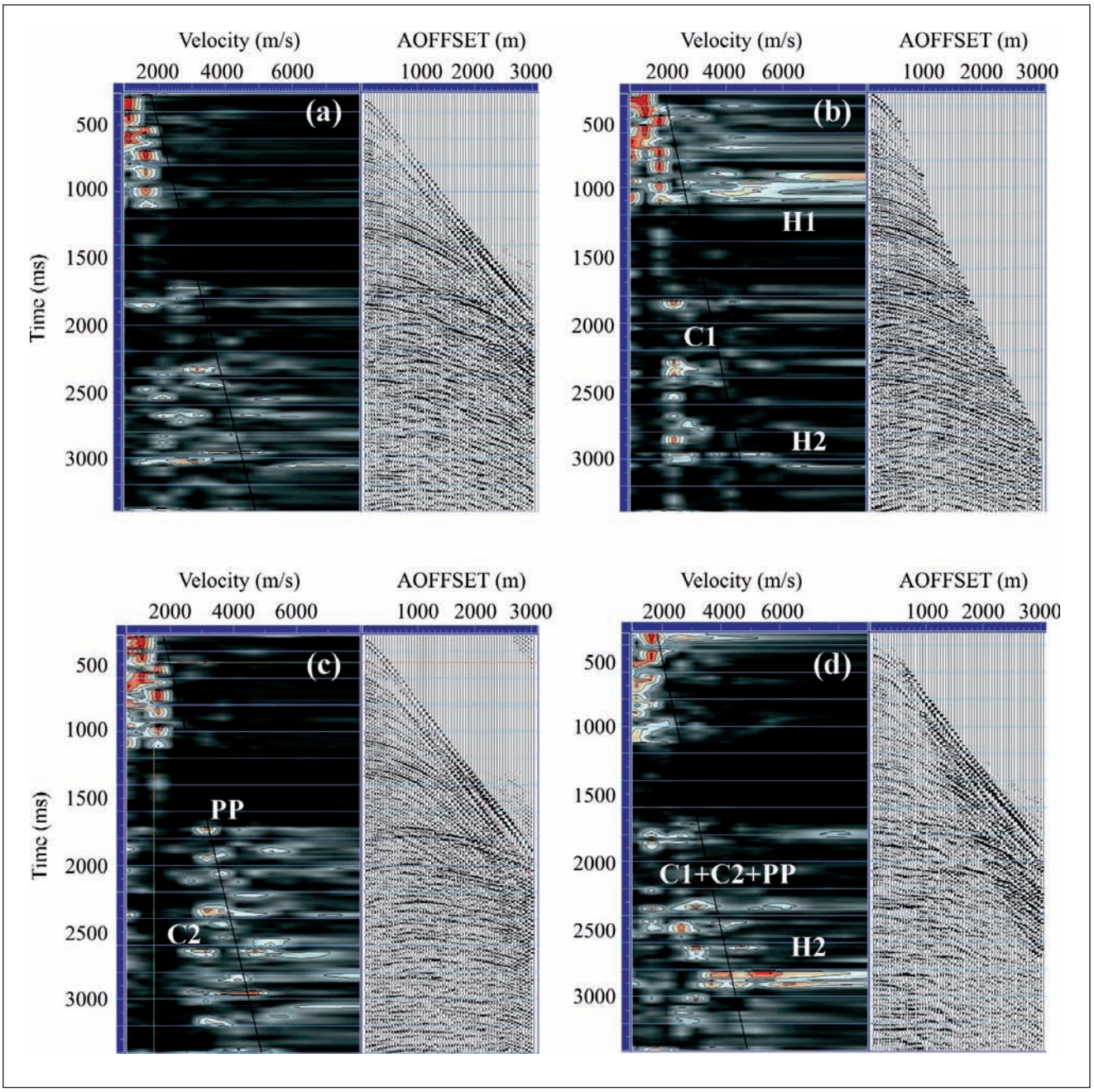


*Figure 10: Example velocity semblance spectra (left) derived from common-shot T-X trace panels (right) before and after signal enhancement and wavefield separation (CMP=1792): (a) input data, (b) GDRT prediction of coherent noise below the TB horizon, (c) GDRT prediction of PP reflections and converted C2 events below the TB horizon and (d) sub-basalt PP signal enhancement using the parabolic Radon transform, as proposed by Spitzer et al. (2003). We focused our attention on the strong and isolated C1, C2 and PP events. Event notations are described in Table 2.*

### *Initial Model Building*

Conventionally, we begin with estimating the reference velocity guide function $V_0(t)$. A comparison of 1D velocity-depth curves derived from sonic logs in Figure 8 demonstrates that the linear gradient model assumption is a reliable approximation of this function similar to the existing regional velocity regression formula of Ogilvie et al. (2001) (see `well data´ section above). Next, points (picks) selected from the velocity semblance panels of pre-processed CMP data, optimally by comparison with QC NMO stacks, are used to generate a time velocity function $V_{stack}(x,\tau_0)$ for stacking and Dix inversion. The Dix inversion formula then transformed the stacking velocity into the reference "sediment-only" velocity perturbation $\Delta V(x,t)$. We also estimate the effective parameter δ using eq. (5), as shown in Figure 11. Confidence limits ("Top/Bottom Delta") of the parameter δ depend on the quality of the seismic-well tie. While noticing rather large uncertainties of the parameter δ beneath the base of the basalt (Figure 11), one would suspect that an inaccurate sub-basalt velocity model might have caused the initially poor image of Cretaceous layers

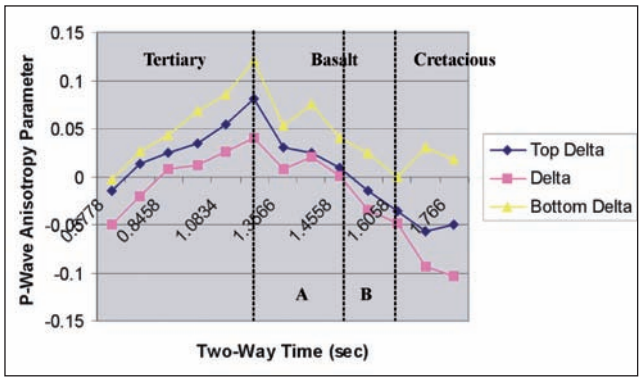


*Figure 11: Thomsen's (1986) delta parameter along with its confidence limits versus Two-Way Time (TWT) referenced to the Seismic Reference Datum (SRD). Zones A and B indicate basic and acid volcanic units, respectively (Figure 6a).*

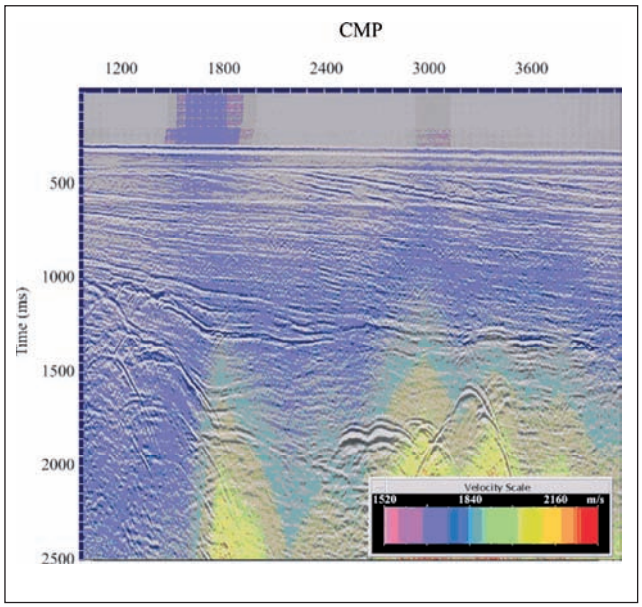


*Figure 12: Results of picking maximum energy from effective velocity scan panels: velocity grids after smoothing and cubic interpolation (in m/s, no actual velocity-contrast interfaces). Input data are prestack CMP gathers (a) before and (b) after GDRT signal enhancement. The velocity model is overlain on the stacked unmigrated section within the CMP range of interest. Grid points were distributed every 12.5 m in the 2D volume. The colour scale enhances maximum and minimum velocities.*

in prestack migration. In this study, non-hyperbolic anisotropic corrections (Thomsen, 1999) did not result in a higher image quality because of the 3 km offset limitation.

### *Time Migration Velocity Model*

The prestack CMP data before and after GDRT are initially migrated using PSTM with the estimated migration velocity $V_{mig}(x,\tau_0) = V^0_{mig}(x,\tau_0) + \Delta V_{mig}(x,\tau_0)$, where $V^0_{mig}(x,\tau_0)$ is the reference migration velocity derived from the stacking velocity $V_{stack}(x,\tau_0)$ (see above sections on reference velocity model and pre-stack time migration); residual curvature on the resulting time-migrated image gathers is used to obtain the velocity update $\Delta V_{mig}(x,\tau_0)$. The resolution of the estimated velocity models in Figures 12a and 12b is low due to smoothing and editing of residual slowness in the velocity update. Aside from this, there is some indication of layering in Figure 12b. It appears that the resulting velocity model in Figure 12b exhibits the regional trend of velocities in the area. This model is more consistent with the interpreted HVL boundaries than that in Figure 12a, suggesting that migration velocity model from the move-out-corrected CMP data after GDRT provides a better fit to the structural interpretation based on regional geophysical data (see section on non-seismic data above). As with RMS velocities, the migration velocities of HVLs in Figure 12 are generally low compared with volcanic interval velocities obtained from the calibrated well data in Figure 6.

### *Prestack Time Migration*

Figures 13a and 13b show a comparison of time migrated CMP data before and after GDRT using the velocity models in Figures 12a and 12b, respectively. As can be seen, the result in Figure 13b demonstrates an improved image of overburden (e.g. events O and EO) and HVL boundaries (TB and BB) when compared with the result in Figure 13a. Notice the significant reduction of high-amplitude

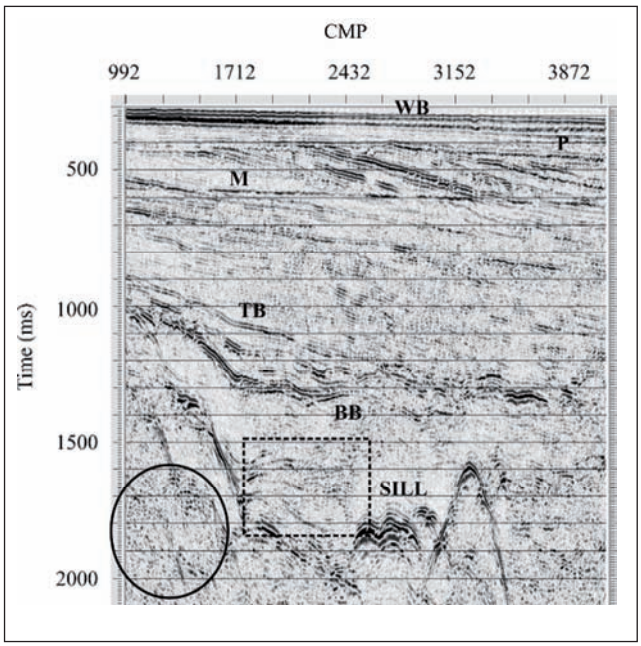


*Figure 13: Results of time processing of prestack CMP data (a) before and (b) after iterative GDRT signal enhancement using velocities in Figures 11a and 11b, respectively. Identical trace scaling (no automatic gain control) was applied to both prestack time-migrated sections. Solid oval and dashed box indicate indicate groups of coherent events that are discussed in the text. These groups contain events C1 and C2 seen in Figures 9b and 9c, respectively. Event notations are described in Table 2.*

coherent noise around the two-way time (TWT) of 1700 ms in Figure 13b (e.g. arrivals C1 and C2 in Figures 10b and 10c), outlined by the solid oval and the dashed box. Analysis suggests well defined HVL boundaries (except the BB geometry in the CDP range 2432-3872) and sufficiently strong intra-basalt reflection coherencies between the TB and BB horizons, acting as efficient PP reflectors and P-to-S energy converters. Despite the residual coherent noise including the seabed PPPP multiple (event M at 560 ms), mode conversions and inter-basalt multiples, an improved time-domain velocity model can be constructed using the image of HVLs in Figure 13b. Although iterative noise attenuation is quite challenging due to relatively sparse source/receiver sampling and offset limitation, it is feasible to identify HVLs acting as efficient energy converters, whereas the interpretation of events outside the prospect region (*CDP*>4833) remains highly ambiguous (not shown). Nevertheless, since migration artefacts and residual noise on the time-migrated unfiltered and filtered data (cf. Figures 13a and 13b) mask the sub-basalt primary PP reflections, there is still not enough confidence to establish that a significant sub-basalt clastic section exists.

*Initial Depth Model Building*

Deficiencies of time processing outlined above reflect the need of depth migration (see subsection on pre-stack depth migration) that can accommodate layers with vastly different elastic properties. We build the initial depth velocity model that consists of layered model-units containing continuous velocity fields (step 1 PSDM). A sufficient number of picked horizons (see WB, P, O, EO, TB, BB, and E1 in Table 2) as well as gridded velocity functions calculated from PSTM (Figure 13b) are used as the starting point for depth-model building. Here, special attention should be paid to unwanted velocity anomalies. If observed, severe smoothing of velocities must be performed. The initial model was weighted by calibrated sonic logs. As with time model building, the parameter $\delta$ (Figure 10) and the velocity trend $V_0(z)$ (Figure 8) are major *a priori* constraints in reducing the misfit between seismic and well-log velocities. Regarding the choice of appropriate time-to-depth mapping, vertical stretching was found to be a poor approximation due to laterally varying high-velocity intervals. Accurate event positioning that accounts for ray bending at layer interfaces was achieved (1) due to the zero-offset oblique-incidence time-to-depth mapping employed (Appendix B) and (2) during migration velocity analysis discussed below.

*Depth Migration Velocity Updating*

Depth velocity updates involve traditional image gather analysis as prescribed previously (steps 2 and 3 PSDM). Here, we follow a basic trial-and-error approach where we test different velocity perturbations $\Delta V(x, z)$ and evaluate the results based on the changes in the offset migrated domain. Namely, the velocity model is perturbed by up to a percentage to select the velocity change that best flattens the image gather. We work to keep the depth interval velocities close to the well velocities in order to minimize time-to-depth conversion errors. It appears that moderate perturbations of the parameter $\delta$ allow us to create a depth-migrated section with accurate reflector depths. Besides, the piecewise constant $V_p/V_s$ ratio is scanned until we achieve the best possible flatness of the P-to-S-to-P image gathers along the key horizons listed in Table 2. We emphasize that this velocity updating process requires pre-processed shot gathers representing output of GDRT wavefield separation (see data pre-processing subsection). The final obtained velocity model for input for the PSDM migration is shown in Figure 14.

To evaluate the benefits contributed by the GDRT wavefield separation, we compare the image gathers obtained from prestack data before and after GDRT for the same CMP location (cf. Figures 15a and 15b). Both were generated with the final velocity model (Figure 14). Clearly, there are significant differences between the image gathers in Figures 15a and 15b. Focusing energy remains diffuse in Figure 15a, making depth model updating more challenging. This diffusion is interpreted to be the result of coherent noise in input prestack data. After the noise was suppressed during pre-processing, the revised image gather in Figure 15b appears to be generally better focused than in Figure 15a, indicating that reflected events are properly placed in the offset-depth migrated domain.

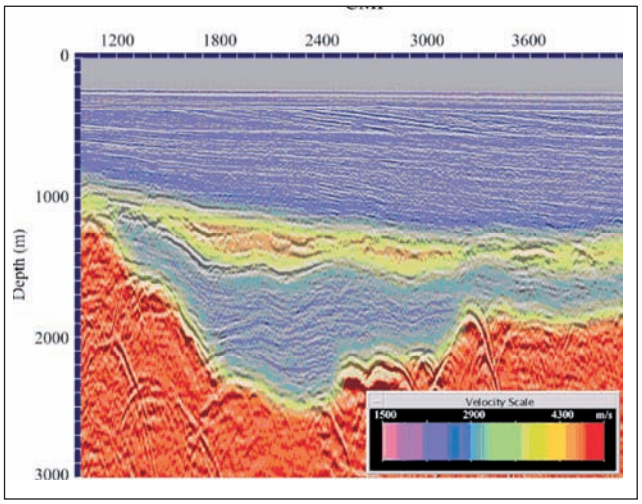


*Figure 14: Depth-domain interval velocity grid model (in m/s) served as the velocity input to PSDM. The velocity model is overlain on the stacked unmigrated section within the CMP range of interest. Principal boundaries of the velocity model are seen. Short-wavelength velocity variations are negligible due to severe smoothness constraints used. See Figure 6a for geological legend.*

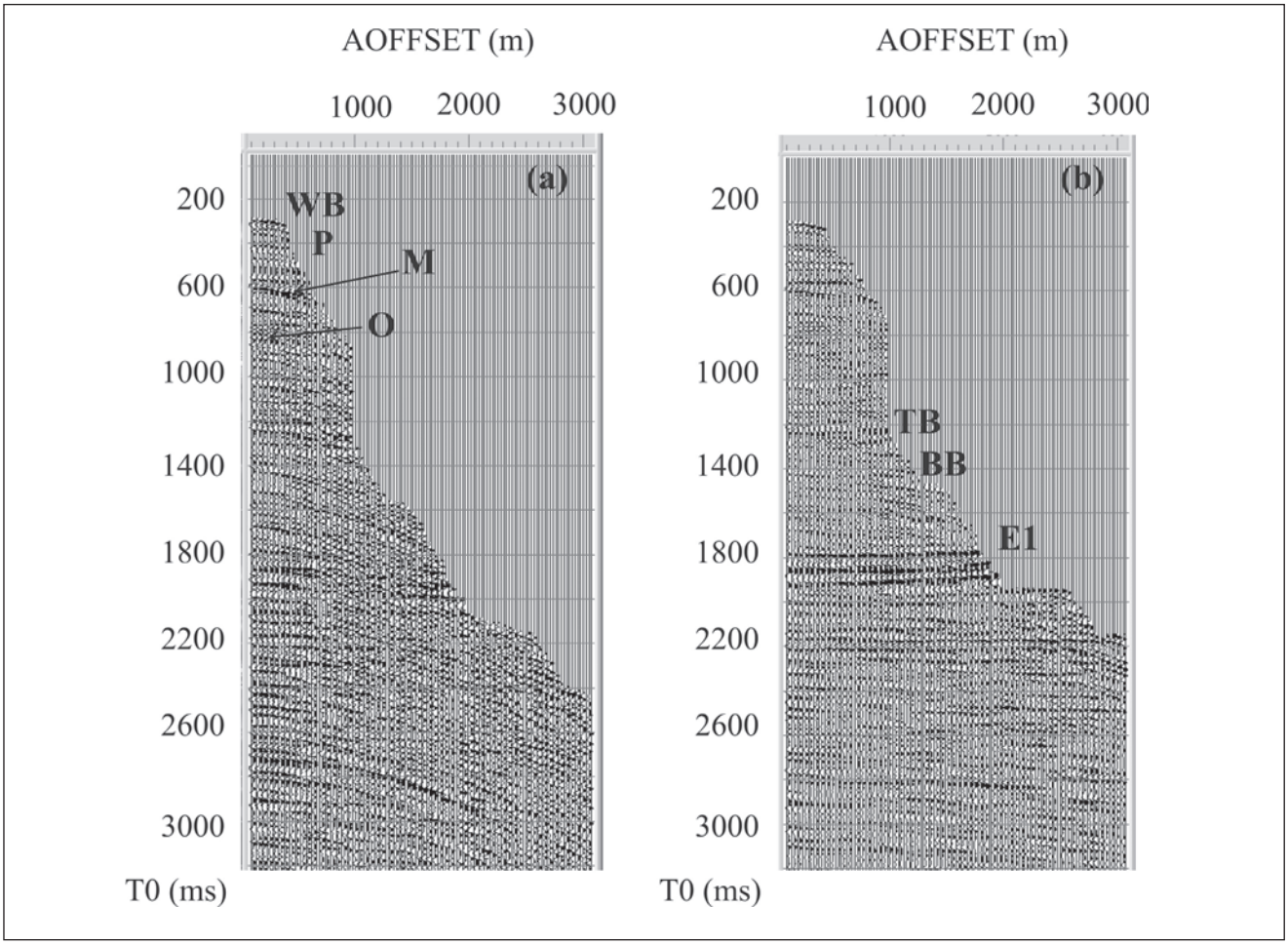


*Figure 15: Example common image gather (CMP=2699) resulting from depth migration of prestack CMP data (a) before and (b) after GDRT signal enhancement. Identical trace scaling (no automatic gain control) was applied to both gathers. For the sake of comparison with time sections in Figure 13, the vertical axis was transformed from the depth domain into the vertical time ($T_0$) domain. We insert additional zero traces into the wiggle-trace panel for display purposes only. Overburden and basalt layers are constrained by sonic logs in Figure 5a and depth-converted horizons picked on the time-migrated section in Figure 12b. Prominent HVL reflections beneath the TB horizon are represented by events E1 (sill reflection) and E2 (basement reflection). The latter is not seen due to noise. Other events are explained in Table 2. Panel (a) shows a significant positive residual moveout (RMO) indicating a general velocity overestimate due to improperly migrated coherent noise. In panel (b), RMO is largely removed due to effective noise attenuation applied.*

*Final Prestack Depth Migration*

We utilize the velocity model from the above velocity update (Figure 14) for the final depth migration. For the sake of simplicity, the migration operator is calculated using the first-arrival ray tracing method augmented with the turning wave option (no evanescent waves). After several iterations, the PSDM process yields the depth image in Figure 16. The overall conclusion is that this velocity model in Figure 14 appears to be sufficiently accurate because the image gather in Figures 15b has negligible residual moveout and stacked events in Figure 16 are well focused. The depth image in Figure 16 is a summation of the PP image and C2-path image after proper least-squares normalization or spectral matching (White, 1980). It shows good event continuity and high resolution in the zone of interest (enclosed by a dashed box in Figure 13), allowing more accurate interpretation of the structure above E1, particularly seismic events associated with the BB horizon and reflections beneath this horizon. Individual volcanic units are clearly imaged by high-amplitude events; amplitudes of events adjacent to intrusions locally decrease, probably reflecting increased crack density (Planke et al., 1999). Also, there exists a reasonable correlation between the intra- and sub-basalt structural discontinuities (possibly, a set of sub-vertical faults related to cooling basalt fractures) observed in Figure 16. Within the target zone ( $992 < CDP < 3332$ and $z \approx 1000$ - 2000 m), the image provides an additional level of detail, giving greater confidence (i.e., lowering risk) in the structural interpretation of the complex HVL structure and sub-basalt reflections. There are a number of (short, coherent) slightly dipping events between the horizons TB and E1. It is not known whether these events are truly sub-horizontal or if they are from out of the plane. Below the depth level of 2200 m, imaging is more problematic since the section is dominated by multiples and other coherent noise seen in Figure 10 and chaotic energy due to incoherent noise (Figure 9).

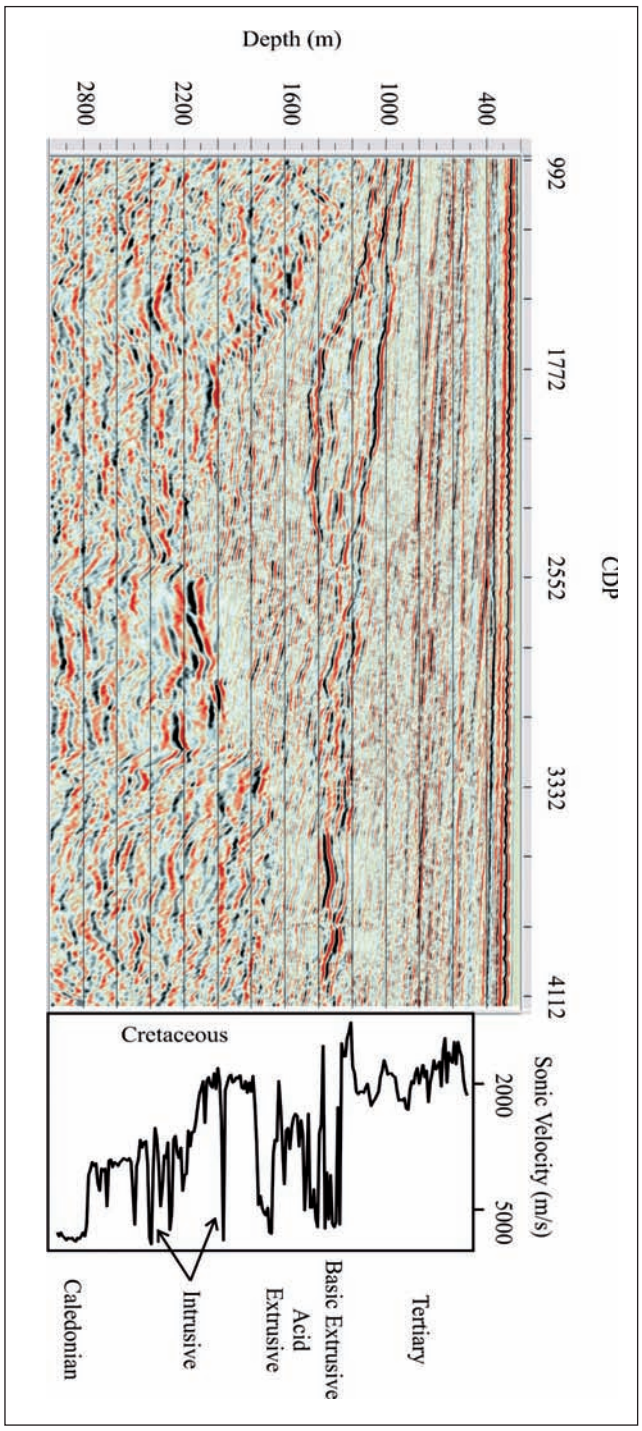


*Figure 16: The final prestack depth-migrated section over the prospect area. Event-based migration was performed after GDRT filtering, trial prestack time migration and migration velocity analysis. This section was generated with the reference velocity model shown in Figure 11b (after time-to-depth conversion). The corresponding common image gather is shown in Figure 13b. The sonic velocity curve (Figure 5a) tied to seismic horizons is attached for lithology discrimination and to support identification of seismic events. Interpretation (TB/BB) is based on horizons derived from prestack time migration (Figure 12b).*

## Discussion

The depth migration results for PP and converted wave modes observed on our data have led to improved focusing on the final PSDM section in Figure 16. To minimize potential destructive interference from different frequency content and kinematics of PP and converted wave modes, we applied the GDRT wavefield separation to input gathers. We also leveraged and stacked multi-mode images to reduce spatial ambiguity, typically observed as coherent noise on individual image gathers due to remaining cross-talk energy. The image in Figure 16 has shown that weak sub-basalt events now can be clearly interpreted as a series of horizons with faults and pinch-outs. Continuous horizons were confirmed by available well information in Figure 6. In contrast, sub-basalt PP reflections in Figure 13 (PSTM) have been poorly focused, and the structure above the event E1 is difficult to interpret. Another technical success in Figure 16 was the perfect match between seismic events in depth and well tops. The accuracy of well tie was within 15 m. Effective Thomsen's (1986) anisotropy and partial coherence matching of images (White, 1980) have played an important role here. Finally, note that both time and depth imaging steps do not rely on a hyperbolic (NMO) approach and other shortcuts associated with conventional time processing (Yilmaz, 2001).

## Conclusions

We have presented an imaging workflow that offers flexibility to migrate the 2D seismic dataset acquired with standard towed cable from the north of Shetland, UK (Figure 5). The critical steps, with respect to the improvements obtained, are the GDRT filtering of prestack gathers, the construction of the velocity model calibrated by sonic logs, and time/depth migration focusing analysis followed by PSDM. The method has the specific advantage that it enables us to enhance individual events associated with HVLs. We choose the model-based methodology described here and assume that *a priori* information is available to generate sufficiently accurate velocity estimates. The joint analysis of log and seismic data demonstrates the ability of the two methods to address imaging issues. We produce a set of image gathers that verify the correctness of the velocity model. We foresee that the best results will be obtained for long-offset seismic profiles because the signal-to-noise ratio of PP reflections and mode conversions at large angles of incidence is better than that of near-offset reflections. Even so, results of this study provide the necessary fast track information to map accurately the radially-dipping structure of the Erlend pluton with consistent intra-basalt reflections. The final image is also capable of imaging subtle features of the surrounding non-volcanic structure beneath the base of basalt.

*Acknowledgements*
The first phase of this project (2000-2004) was supported by the EC-funded research project SIMBA coordinated by Total. The second phase (2004-2005) was funded by the following sponsors of the British Geological Survey (BGS/NERC): BG, BGP, BP, Chevron, ConocoPhillips, CNPC, ENI-Agip, ExxonMobil, GX Technology, Kerr-McGee, Landmark, Marathon, Norsk Hydro, PDVSA, Shell, Schlumberger, Total, and Veritas DGC. It is published with the permission of the BGS, SIMBA partners and industrial sponsors. We are grateful to Norsk Hydro for agreeing to release seismic data. Fugro Robertson Ltd. prepared well log data for us in accordance with the UK Trade Partners agreement. We acknowledge the administrative support of Paul Williamson (Total), Colin MacBeth (Heriot-Watt University) and Xiang-Yang Li (BGS). We also thank Phil Christie (Schlumberger) and two anonymous reviewers of the paper. Their comments have been very helpful in improving the clarity and readability of the paper.

## References

Baan, van der M., Kerrane, T., Kendall, J-M., Taylor, N., 2003. Imaging sub-basalt structures using locally converted waves. *First Break 21*, 29-36.

Barzaghi, L., Calcagni, M., Passolunghi, M., Sandroni, S., 2002, Faeroe sub-basalt seismic imaging: a new iterative time processing approach. *First Break 20,* 611-617.

Dillon, P. B., Ahmed, H., Roberts, T., 1988. Migration of mixed mode VSP wavefields. *Geophysical Prospecting 36*, 825-846.

Droujinine, A., 2005. The attribute based generalized discrete Radon transform. Journal of *Seismic Exploration 14,* 155-196.

Gatliff, R.W., Hitchen, K., Ritchie, J.D., Smythe, D.K., 1984. Internal structure of the Erlend Tertiary volcanic complex, north of Shetland, revealed by seismic reflections. *Journal of the Geological Society 141*, 555-562.

Hawkins, K., Leggott, R., Williams, G., Kat, H., 2001. Addressing anisotropy in 3-D prestack depth migration: A case study from the Southern North Sea. *The Leading Edge 20*, 528-535.

Jolley, D. W. and Bell, B. R., 2002. Genesis and age of the Erlend Volcano, NE Atlantic Margin: *Geological Society, London, Special Publications 197*: 95-110.

Jones, I.F., 2003. A review of 3D preSDM velocity model building techniques. *First Break 21*, 45-58.

Kuo, J. T., and Dai, T-F., 1984. Kirchhoff elastic migration for the case of noncoincident source and receiver, *Geophysics 49*, 1223-1238.

Lambaré, G., Herrmann, P., Guillaume, P., Zimine, S., Wolfarth, S., Hermant, O., Butt, S., 2007. From time to depth imaging with 'Beyond Dix'. *First Break 25,* 71-76.

Lokshtanov, D., 1999. Multiple suppression by data-consistent deconvolution. *The Leading Edge 18*, 115-119.

Maeland, E., 1997. Focusing analysis of seismic data with peg-leg multiples. *Geophysics 62*, 177-182.

Maresh, J., White, R.S., 2005. Seeing through a glass, darkly: strategies for imaging through basalt. *First Break 23*, 27-33.

Martini, F., Bean, C. J., 2002. Interface scattering versus body scattering in sub-basalt imaging and application of prestack wave equation datuming. *Geophysics 67*, 1593-1601.

Ogilvie, J. S., Crompton, R., Hardy, N. M., 2001. Characterization of volcanic units using detailed velocity analysis in the Atlantic Margin, West of Shetlands, United Kingdom. *The Leading Edge 20*, 34-50.

Planke, S., Alvestad, E., Eldholm, O., 1999. Seismic characteristics of basaltic extrusive and intrusive rocks. *The Leading Edge 18*, 342-348.

Purnell, G. W., 1992. Imaging beneath a high-velocity layer using converted waves. *Geophysics 57,* 1444-1452.

Robein, E., Hanitzsch, C., 2001. Benefits of pre-stack time migration in model building: a case history in the South Caspian Sea. *First Break 19*, 183-189.

Spitzer, R., White, R. S., Christie, P. A. F., 2003. Enhancing sub-basalt reflections using parabolic $\tau$ - $p$ transformation. *The Leading Edge 22*(12), 1184-1201.

Stoker, M.S., Hitchen, K., Graham, C.C., 1993. The geology of the Hebrides and West Shetland shelves, and adjacent deep-water areas. HMSO, London.

Tabti, H., Gelius, L-J., Hellmann, T., 2004. Fresnel aperture prestack depth migration. *First Break 22*, 39-46.

Thomsen, L., 1986. Weak elastic anisotropy. *Geophysics 51,* 1954-1966.

Thomsen, L., 1999. Converted-wave reflection seismology over inhomogeneous, anisotropic media. *Geophysics 64,* 678-690.

White, R. E., 1980. Partial coherence matching of synthetic-seismograms with seismic traces. *Geophysical Prospecting 28*, 333-358.

Yilmaz, O., 2001. Seismic data analysis. SEG, Tulsa, OK.

## Appendix A: GDRT wavefield separation

Primaries and multiples can be separated in the parabolic Radon domain because of their different RMS velocities (Spitzer et al., 2003). Similarly, event separation can be achieved by means of local moveout operators, used to increase the PP-wave signal-to-noise ratio and to identify non-PP events not interpretable on the PP sections. The GDRT filter is applied to common-midpoint (CMP), common-source (CS) or common-receiver (CR) gathers. Assuming the offset domain, we compute a model of primary and multiple events by taking into account the above local traveltime approximations. The GDRT algorithm finds a representation in the model domain (Figure 2) that, in a least-squares sense, describes the input data best. The justification for event modelling is that it allows separation of principal arrivals described in Table 2. GDRT represents data decomposition into user-defined parabolic (beam-stack) segments using the least squares method in the frequency-space domain (F-X) for each frequency of the band defined by $f_{min}$ and $f_{max}$. According to the elastic Huygens' principle (Kuo and Dai, 1984), GDRT simulates the input data as a linear combination (superposition) of the individual wave modes (PP, converted waves, refractions, etc.). The data are split into several frequency bands, the detection occurs in the higher bands, and a selective attenuation is made so as to preserve the lower bands, which contain more primary energy. The GDRT decomposition consists in carrying out semblance scans (stacks) according to the various values of the ($P$-$Q$) attributes in eq. (A1), then a spatial deconvolution of the obtained spectrum. The scan of parabolas is defined by the position ($\tau$,$X_0$) and an increment between parabolas ($\Delta\tau$, $\Delta\tau$). The user also specifies the ($P$-$Q$) attribute lower-upper limits and increments ($P_{\min}$, $P_{\max}$), ($Q_{\min}$, $Q_{\max}$) and ($\Delta P$, $\Delta Q$). The attribute range and increment values are chosen so that it is possible to separate events of interest and to eliminate alias contributions while still including undistorted events passed by a given window function. The events are defined by the (pass or reject) sub-range or threshold values ($P^0_{\min}$>$P_{\min}$, $P^0_{\max}$< $P_{\max}$), ($Q^0_{\min}$>$Q_{\min}$, $Q^0_{\max}$< $Q_{\max}$) or ($P_0$, $Q_0$). For example, events corresponding to parabolas with the $Q$-attribute greater than the threshold $Q_0$ can be

considered as multiples, whilst events corresponding to parabolas smaller than this threshold can be deemed to be primary events. The difference between data and the sum of modelled events is interpreted as residual noise. In practice, the "multiple-only" gather often contains some residual primary energy and vice versa (Yilmaz, 2001). GDRT subtracts from the input gather the model of events or the individual event plus the residual noise. During event identification and velocity analysis sessions, GDRT enables users to view the (*P*-*Q*) attribute (two-parameter) semblance panels of Droujinine (2005) as conventional (single-parameter) effective velocity spectra. GDRT offers the following benefits: (1) analysis may be carried out on an existing grid of CMP locations as commonly defined for RMS velocity scans, (2) it may speed laborious event picking on large projects without decreasing event resolution, and (3) it eases quality control of the global reflection moveout (Yilmaz, 2001) or its anisotropic counterpart (Thomsen, 1999) within a user specified offset range.

## Appendix B: zero-offset time-to-depth mapping

Assume that we have determined the set $\Sigma_n^\tau : (X_n, \tau_n)$, $n = 1,2,\ldots N$, of zero-offset traveltimes $\tau = \tau_0$ of primary reflections, as sketched in Figure 4a. Our objective is to define a transformation (time-to-depth mapping) of the set $\Sigma_n^\tau$ on the plane ($X$, $\tau$) (time domain) into the set $\Sigma_n^z$ on the plane ($X$, $Z$) (depth domain) using the given velocity model $V_n = V(X_n, \tau_n)$ and the slope field $p_n = \partial\tau / \partial X_n$ or the local dip field $d_n = V_n \partial\tau / \partial X_n$ measured in the time domain. This transformation can be implemented in the following recursive (layer-stripping) manner. According to the zero-offset Huygens' principle ("exploding reflector" scenario), each point $(X_{n-1}, Z_{n-1})$ of the reflector $\Sigma_{n-1}^z$ can be considered as an origin (secondary source) of a secondary wavefront with the radius $r_{n-1} = V_{n-1}(\tau - \tau_{n-1})$, and the corresponding diffraction hyperbola $\Omega_{n-1}$ can be represented as $(X - X_{n-1})^2 + (Z - Z_{n-1})^2 = r_{n-1}^2$ (Figure 4b) in the depth domain. If $N$ secondary sources are considered, the envelope of a system of secondary wavefronts $\Omega_{n-1}$ constitutes the interface $\Sigma_n^z$ given parametrically $X = X_{n-1} - r_{n-1} d_{n-1}$ and $Z = Z_{n-1} + r_{n-1}\sqrt{1 - d_{n-1}^2}$. This is the known process of zero-offset kinematic migration (Maeland, 1997) that properly collapses time-domain diffraction events and transforms the set of dip segments $(X_n, \tau_n, d_n)$ in the time domain into the set of continuous interfaces $\Sigma_n^z$ in the depth domain. In the present study, this process is constrained by the control points in Figure 7 and by the regional trend in Figure 8.